

Supporting Information for Pushing the Limit of High-Q Mode of a Single Dielectric Microcavity

Lujun Huang^{a,+}, Lei Xu^{b,+}, Mohsen Rahmani^b, Dragomir Neshev^c, and Andrey E Miroshnichenko^{a,*}

+ These authors contributed equally.

*Corresponding Author: E-mail: andrey.miroshnichenko@unsw.edu.au

^aUniversity of New South Wales, School of Engineering and Information Technology, Canberra, Australian Capital Territory, Australia

^bNottingham Trent University, School of Science and Technology, Department of Engineering, Advanced Optics and Photonics Laboratory, Nottingham, United Kingdom

^cThe Australia National University, Research School of Physics, Department of Electronic Materials Engineering, ARC Centre of Excellence for Transformative Meta-Optical Systems (TMOS), Canberra, Australian Capital Territory, Australia

Section 1-4

Table.S1-S4

Figure.S1-28

Section 1-Two level system for BIC and QBIC

The fundamental physics behind can be described by 2*2 Hamiltonian matrices describing two coupled modes, which has been discussed explicitly in Ref [14]. The formula is given as follows

$$H = \begin{pmatrix} E_1 & V \\ W & E_2 \end{pmatrix} \quad (1)$$

where E_1 and E_2 are the complex energies of the uncoupled system; V and W are the coupling constants. For an open system, all the parameters are complex, in general, and describe the interaction of leaky modes. The eigenvalues of the matrix can be obtained by diagonalization of the matrix, and are expressed as follows

$$E_{\pm} = \frac{E_1 + E_2}{2} \pm \sqrt{\frac{(E_1 - E_2)^2}{4} + VW} \quad (2)$$

Note that the imaginary parts of E_{\pm} correspond to the decay rate of the coupled modes. The Q-factor for coupled and uncoupled modes are $Q_{\pm} = -\text{Re}(E_{\pm}) / (2 \times \text{Im}(E_{\pm}))$ and $Q_{1,2} = -\text{Re}(E_{1,2}) / (2 \times \text{Im}(E_{1,2}))$, respectively. For the sake of simplicity and without loss

of generality, we assume $E_1 = E_0 - \gamma_0 i$ and $E_2 = E_0 + \Delta - \gamma_0 i$, where γ_0 is the radiative rate of two uncoupled modes, and Δ is the frequency detuning, assumed to be real. The Eq.(2) can be further simplified as

$$E_{\pm}(\Delta) = E_0 + \frac{\Delta}{2} - \gamma_0 i \pm \sqrt{\frac{\Delta^2}{4} + VW} \quad (3)$$

By properly engineering the complex coupling VW , one may make the radiative decay rate for one mode as zero, which also means the infinite Q-factor (matching the definition of BIC). However, when complex coupling deviates from this critical value, ideal BIC will be converted into quasi-BIC. Fig.S1 gives one example of BIC and QBIC for two level systems with different value of complex coupling.

Section 2-Derivation of ray optics model

Apparently, the high Q modes, such as $TE(m, m+2)$ and $TE(m, m+1)$, has a diamond shape. In the following section, we use high Q mode $TE(m, m+2)$ as an example to illustrate the ray optics model. The resonant frequency of high Q modes can be estimated by using the localization of ray^{14,28}. The total phase shift of the dielectric resonator can be expressed as follows

$$\frac{4\pi n a \sqrt{1+R^2}}{\lambda} - \beta = 2\pi(m + m + 2) \quad (4)$$

Where a is the width of rectangular NW, n is the refractive index of NW, R is the critical size ratio and λ is the resonant frequency of NW. Note that the first term in Eq.(4) corresponds to the phase shift generated by rays travelling inside the resonator. The second term β is the phase induced by the reflection at the dielectric boundary, and can be expressed by

$$\beta = 4(\arctan\alpha_1 + \arctan\alpha_2) \quad (5a)$$

$$\alpha_1 = \frac{\sqrt{n^2 \sin^2 \theta_1 - 1}}{n \cos \theta_1} \quad (5b)$$

$$\alpha_2 = \frac{\sqrt{n^2 \sin^2 \theta_2 - 1}}{n \cos \theta_2} \quad (5c)$$

in which $\tan \theta_1 = 1/R$, and $\theta_2 = \pi/2 - \theta_1$.

Combing eq.(4) and eq.(5), we can obtain

$$\frac{a}{\lambda} = \frac{1}{n\sqrt{1+R^2}} \left(m + 1 + \frac{\beta}{4\pi} \right) \quad (6)$$

Since the critical size ratio changes mildly, we can find that a/λ shows linear dependence on the mode order m . Fig.S5 shows the a/λ as a function of mode order m for both high Q modes $TE(m, m+2)$ and $TE(m, m+1)$. Good agreement can be found between numerical results based on FEM method and analytical results obtained from ray optics model.

Section 3-Rabi-split of high and low Q modes for TE and TM cases

For coupled two resonant modes, the complex eigenvalues of modes are

$$E_{\pm} = \frac{E_1 + E_2}{2} \pm \sqrt{\frac{(E_1 - E_2)^2}{4} + VW} \quad (7)$$

When $\text{real}(E_1) = \text{real}(E_2)$

$$2 \hbar \Omega = 2 \sqrt{VW - \frac{(E_{1i} - E_{2i})^2}{4}} \quad (8)$$

When $2\Omega > 0$, avoid crossing of two modes is expected. For strong coupling regime, it is required $2\Omega > (\gamma_1 + \gamma_2)$. When $2\Omega \leq 0$, these two modes will cross with each other. Therefore, we define the coupling strength between two modes as $C = 2\Omega / (\gamma_1 + \gamma_2)$. Table S2 lists coupling strength between high and low Q modes for both TE and TM cases

Section 4-Fano resonance fitting of experimental scattering spectrum

Since the scattering spectrum shows Fano resonance features³², we use the following equation to fit the scattering to extract the resonant frequency and quality factor,

$$\sigma_{sc} = \sigma_{bg} + A \frac{(q\gamma_0 + \omega - \omega_0)^2}{\gamma_0^2 + (\omega - \omega_0)^2} \quad (4)$$

in which γ_0 and ω_0 are the damping rate and resonant frequency of the mode and q is the Fano parameters, A is the amplitude of the resonance.

Table S1 Pairs of high Q and Low Q modes in single rectangular NW for TE case

TE(m,l)	High Q mode	Low Q mode	Critical Ratio
Type I: $l=m+2$	TE($m,m+2$)	TE($m+2,m$)	$R_0=1$
Type II: $m \leq l < m+2$	TE(m,l)	TE($m+2,l-2$)	$0 < R_0 < 1$
Type III: $l > m+2$	TE($m+2,l-2$)	TE(m,l)	$R_0 > 1$
Type IV: $m > l$	same as TE(l,m)	same as TE($l+2,m-2$)	$1/R_0$

Note: eigenvalue $nka(a=b/R)$ for TE(m,l) ($m > l$) is same as eigenvalue nkb for TE(l,m), and thus the critical ratio becomes $1/R_0$, where R_0 is critical ratio for TE(l,m)

Table S2. Coupling strength between high and low Q modes for single NW

Modes	m=1	m=2	m=3	m=4
TE($m,m+2$)	0.3764	1.5856	2.4249	1.8641
TE($m+2,m$)				
TE($m,m+1$)	---	0.7080	1.8217	2.0804
TE($m+2,m-1$)				
TE(m,m)	---	---	0.6330	1.4843
TE($m+2,m-2$)				
TM($m,m+2$)	---	0.2396	1.3427	0.1662
TM($m+2,m$)				
TM($m,m+1$)	---	-0.1788	0.0207	0.5356
TM($m+2,m-1$)				
TM(m,m)	---	---	-0.0369	-0.0022
TM($m+2,m-2$)				

Table S3. Coupling strength between high and low Q magnetic modes in single disk and cuboid

Shape	Mode	m=2	m=3
3D Disk	M(1,m,m+2)	2.0192	---
	M(1,m+2,m)		
	M(1,m,m+1)	0.7387	---
	M(1,m+2,m-1)		
	M(1,m,m)	---	0.5298
	M(1,m+2,m-2)		
3D Cuboid	M(1,m,m+2)	2.0853	---
	M(1,m+2,m)		
	M(1,m,m+1)	0.6259	
	M(1,m+2,m-1)		
	M(1,m,m)	---	0.3572
	M(1,m+2,m-2)		

Table S4. Coupling strength between high and low Q electric modes in single disk and cuboid.

Shape	Mode	m=1	m=2
3D Disk	E(1,m,m+2)	---	0.4076
	E(1,m+2,m)		
	E(1,m,m+1)	---	-0.1570
	E(1,m+2,m-1)		
3D Cuboid	E(1,m,m+2)		1.0257
	E(1,m+2,m)		
	E(1,m,m+1)		-0.6237
	E(1,m+2,m-1)		

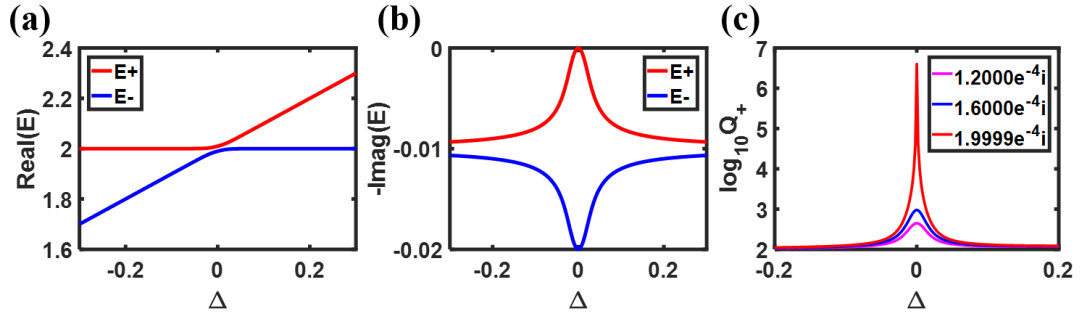


Figure S1. BIC mode and QBIC mode in the two-level system. (a-b), Real and imaginary part of eigenvalues E_{\pm} as a function of Δ for $E_1=2-0.01i$ and $E_2=2+\Delta-0.01i$ and $VW=2.0e-4i$. (c), The Q-factor of mode E_{+} as a function of Δ when complex coupling varied from $1.2 \times 10^{-4}i$ to $1.9999 \times 10^{-4}i$.

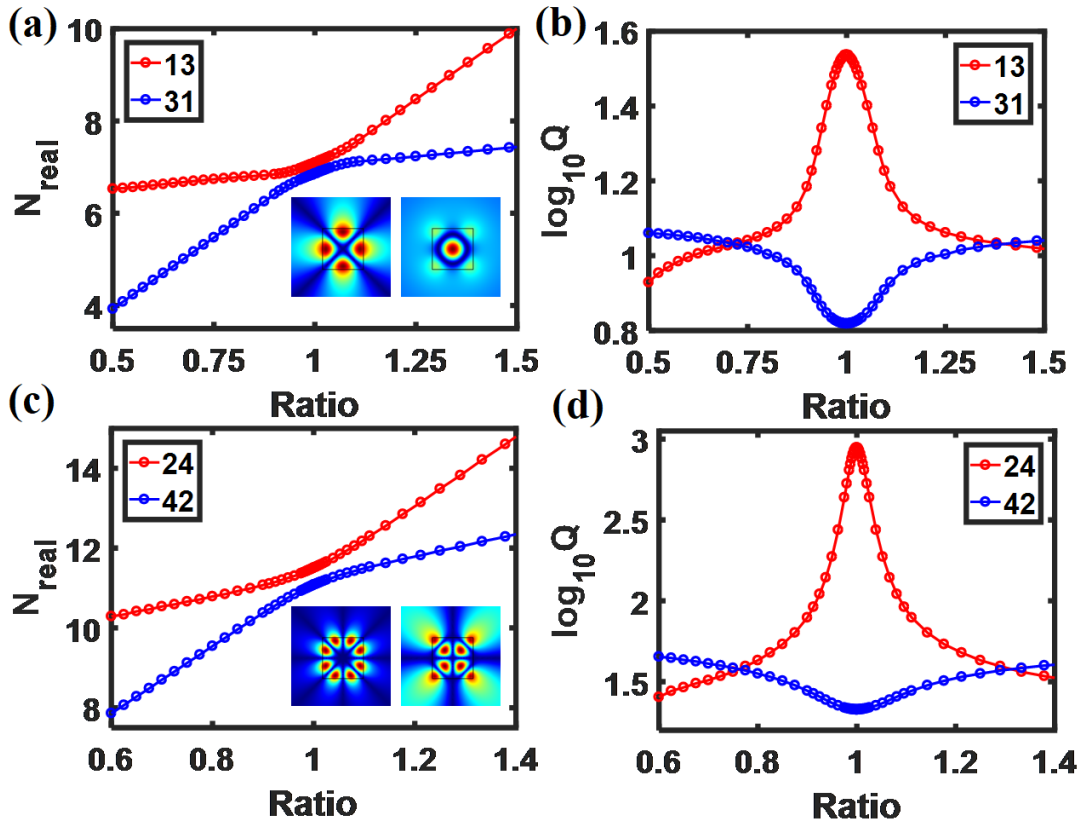


Figure S2. High Q mode $TE(m,m+2)$. a-b, Real part and Q factor of eigenvalue for modes $TE(1,3)$ and $TE(3,1)$ as functions of size ratio R . c-d, Real part and Q factor of eigenvalue for modes $TE(2,4)$ and $TE(4,2)$ versus size ratio R .

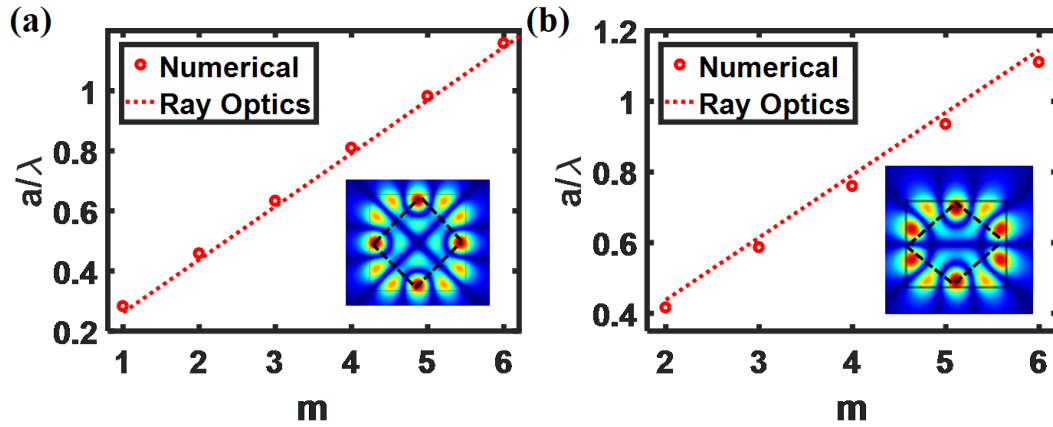


Figure S3. Physical explanation of linear dependence of a/λ on m for high Q mode. a, numerical results based on FEM and Analytical results based on ray optics for mode $TE(m,m+2)$. b, numerical results based on FEM and Analytical results based on ray optics for mode $TE(m,m+1)$.

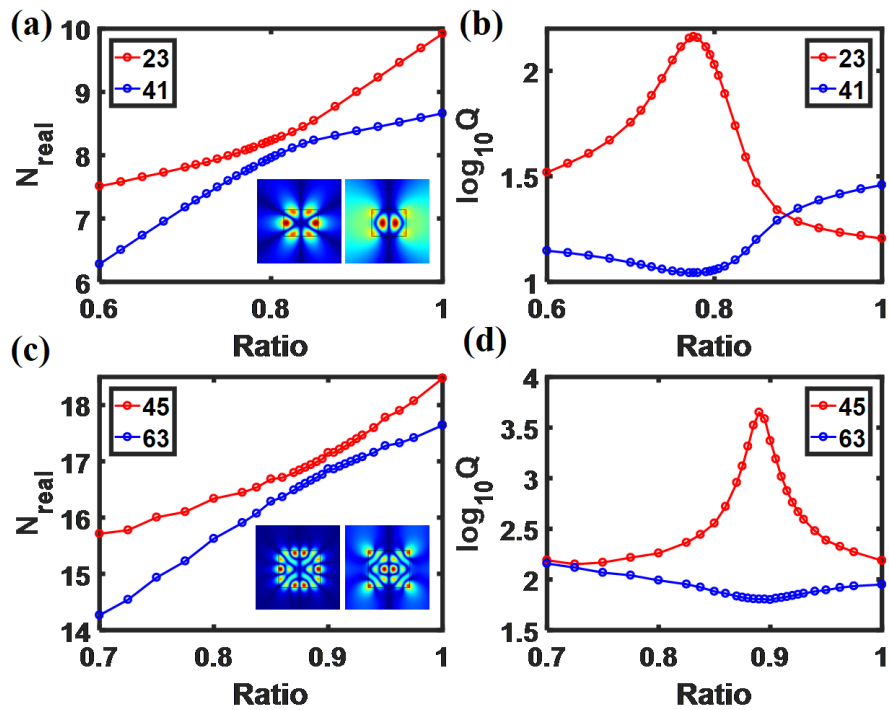


Figure S4. High Q mode $TE(m,m+1)$. a-b, Real part and Q factor of eigenvalue for modes $TE(2,3)$ and $TE(4,1)$ as functions of size ratio R . c-d, Real part and Q factor of eigenvalue for modes $TE(4,5)$ and $TE(6,3)$ versus size ratio R .

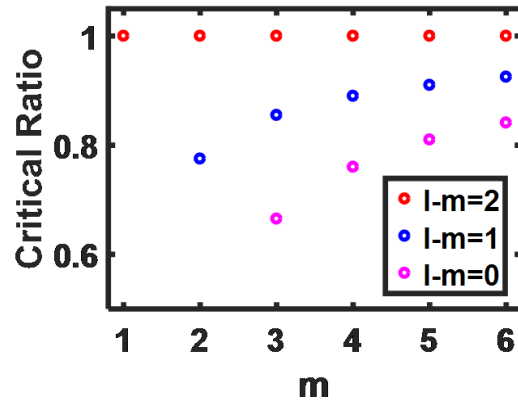


Figure S5. Critical size ratio as function of m for mode $TE(m, m+2)$, $TE(m, m+1)$, and $TE(m, m)$.

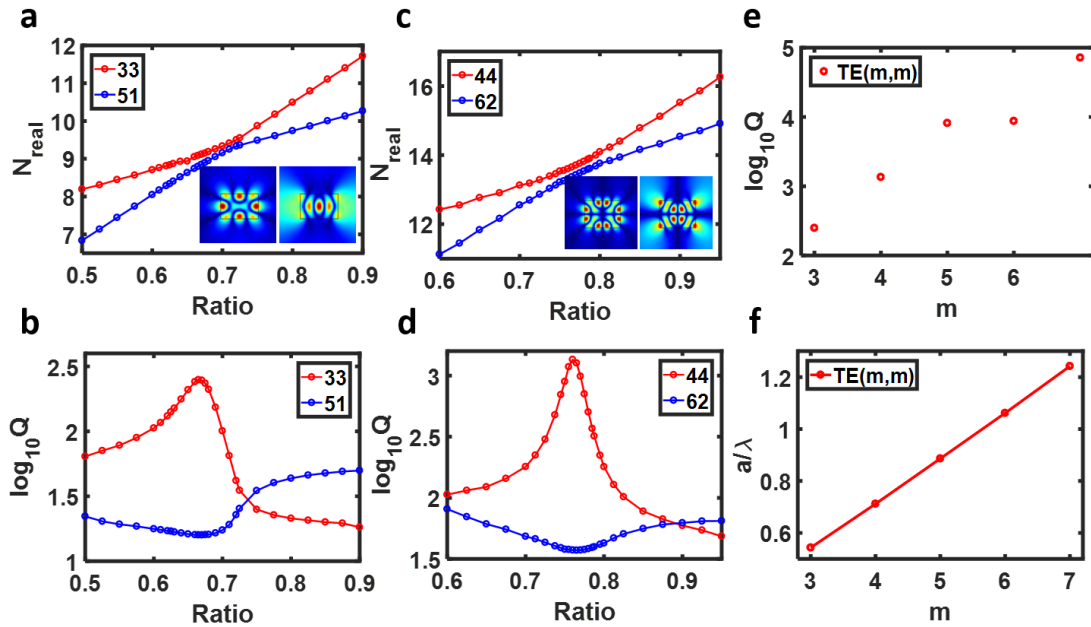


Figure S6. **a-b**, Real part and Q-factor of the eigenvalue of modes $TE(3,3)$ and $TE(5,1)$ (Type II) as functions of size ratio R . **c-d** Real part and Q-factor of the eigenvalue of modes $TE(4,4)$ and $TE(6,2)$ (Type II) as functions of size ratio R . **e-f**, Q-factor and a/λ as functions of m for high-Q mode $TE(m, m)$ at the critical ratio.

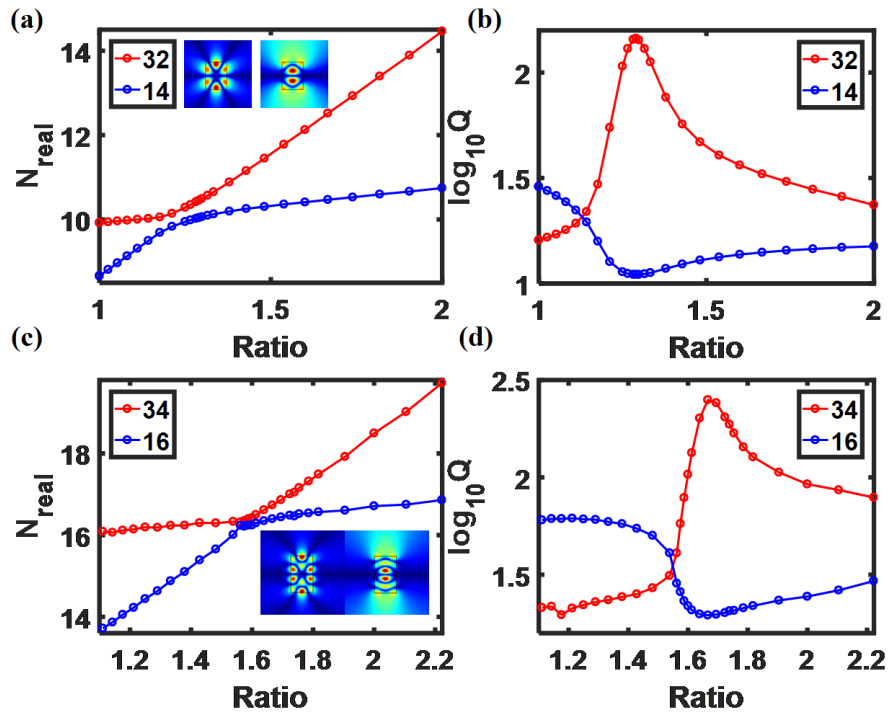


Figure S7. a-b, Real part and Q factor of eigenvalue for modes TE(3,2) and TE(1,4) as functions of size ratio R . c-d, Real part and Q factor of eigenvalue for modes TE(3, 4) and TE(1,6) versus size ratio R .

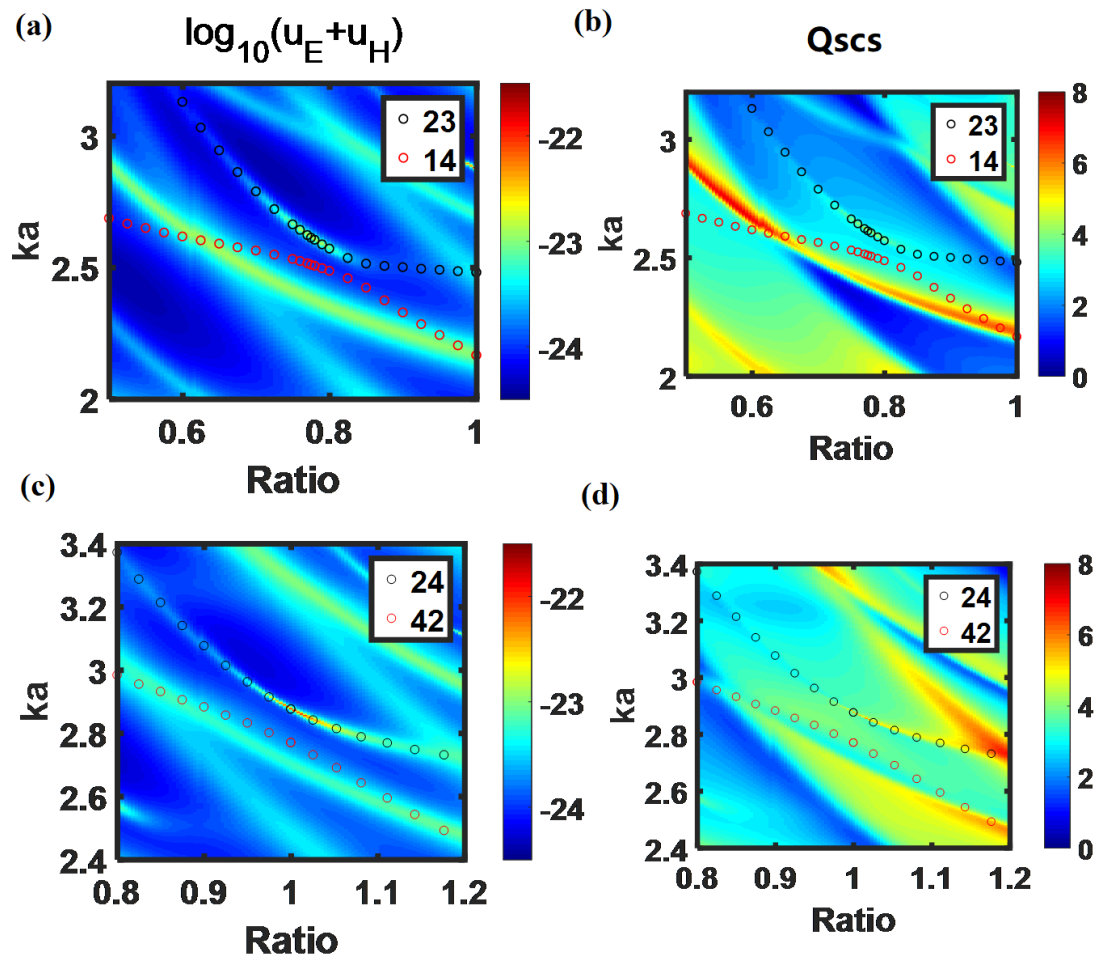


Figure S8. Total Energy density and scattering efficiency for rectangular NW with different size ratio. a-b, Logarithm total energy density and scattering efficiency mapping versus R and ka . Two mode TE(2,3) and TE(4,1) are labeled as black and red circles. c-d, Logarithm total energy density and scattering efficiency mapping versus R and ka . Two mode TE(2,4) and TE(4,2) are labeled as black and red circles.

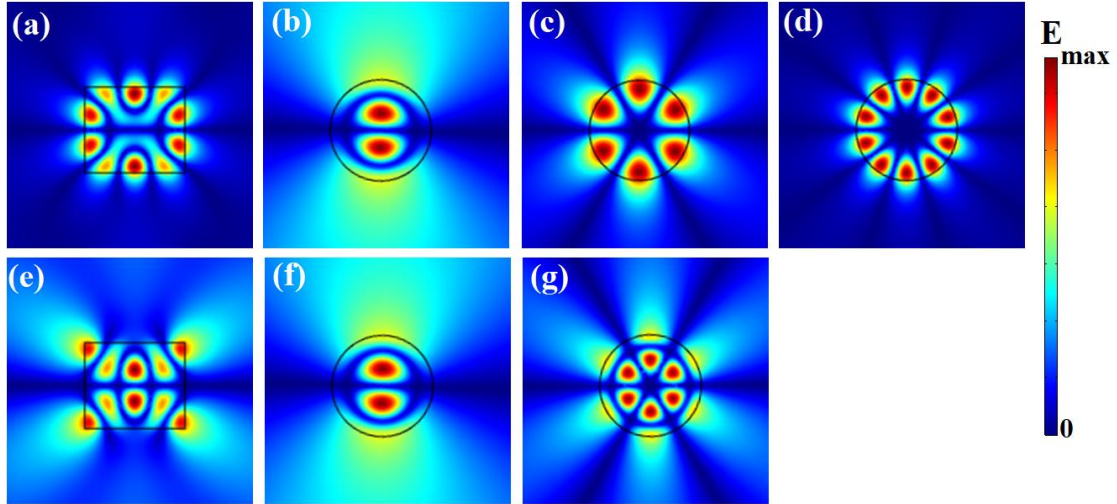


Figure S9. Eigenfield Distribution of high Q mode for rectangular NW and orthogonal eigenchannels in circular NW. a-c, eigenmode TE(3,4) and its eigenchannels TE₁₂,TE₃₁,TE₅₁. d-f, eigenmode TE(5,2) and its two eigenchannels TE₁₂,TE₃₂.

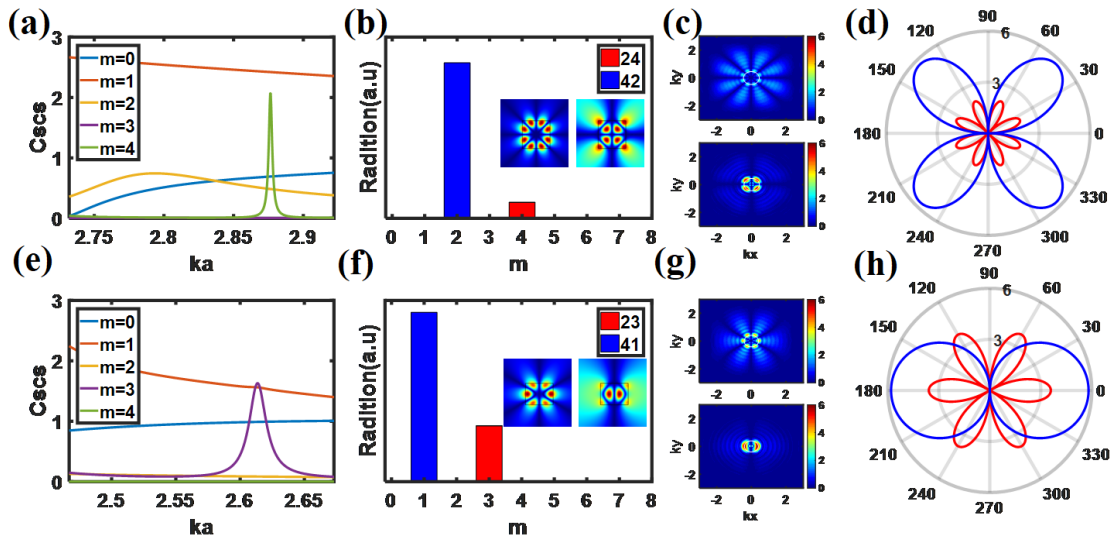


Figure S10. Physical explanation of high Q modes. **a**, Multipolar contribution on scattering cross section of the square NW under the excitation oblique incidence plane wave ($\theta=15^\circ$). **b**, Multipole analysis on the eigenfields of two modes TE(2,4) and TE(4,2). **c**, $E(k)$ mapping obtained from Fourier transformation of eigenfields for two modes. **d**, $E(k_0)$ extracted from $E(k)$ mapping at $k=k_0$. **e**, Multipolar contribution on scattering cross section of the rectangular NW with $R=0.855$ under the excitation oblique incidence plane wave ($\theta=15^\circ$). **f**, Multipole analysis on the eigenfields of two modes TE(2,3) and TE(4,1). **g**, $E(k)$ obtained from Fourier transformation of eigenfields for two modes. **h**, $E(k_0)$ extracted from $E(k)$ mapping at $k=k_0$.

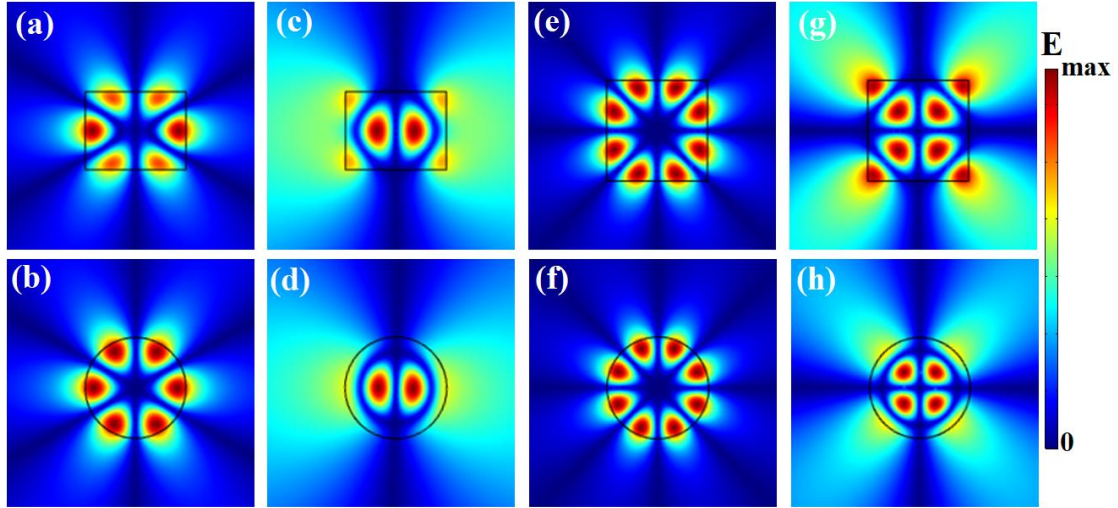


Figure S11. Eigenfield Distribution of high Q mode for rectangular NW and orthogonal eigenchannels in circular NW. a-b, eigenmode TE(2,3) and its eigenchannel TE₃₁. c-d, eigenmode TE(4,1) and its eigenchannel TE₁₂. e-f, eigenmode TE(2,4) and its eigenchannel TE₄₁. g-h, eigenmode TE(4,2) and its eigenchannel TE₂₂.

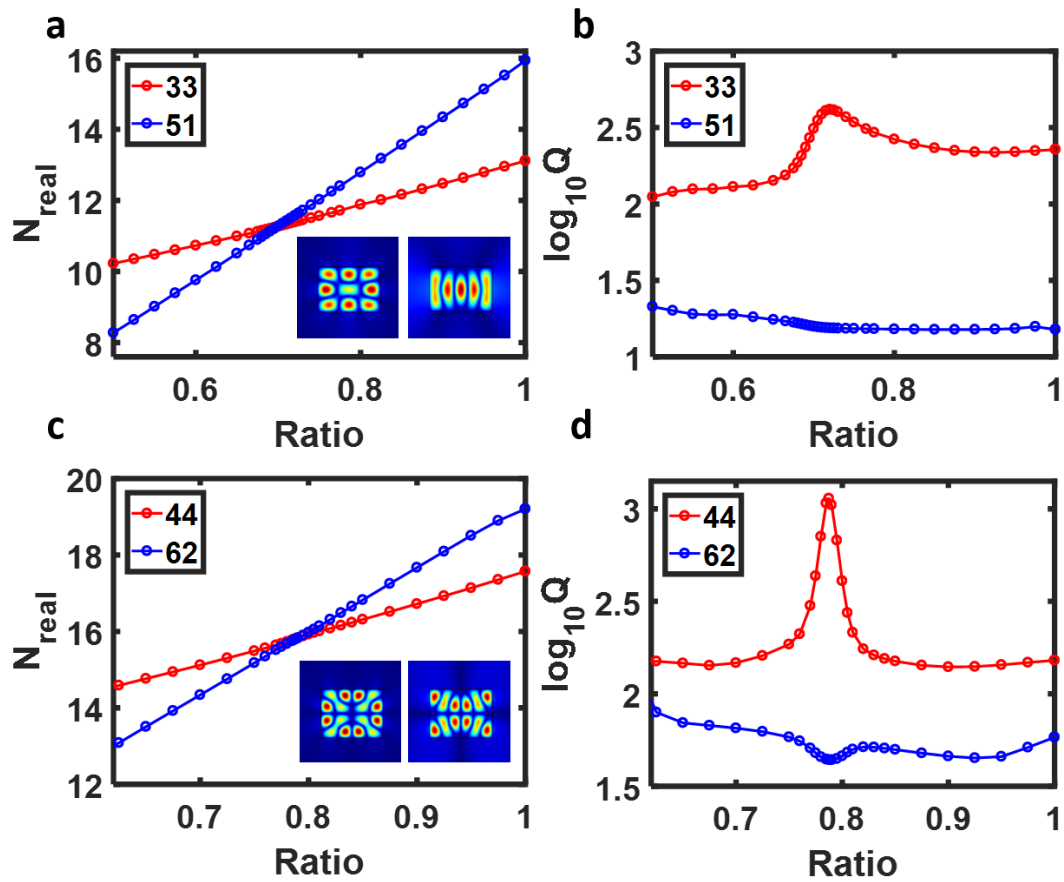


Figure S12. a-b, Real part and Q factor of eigenvalue for modes TM(3, 3) and TM(5,1) versus size ratio R. c-d, Real part and Q factor of eigenvalue for modes TM(4, 4) and TM(6,2) versus size ratio R.

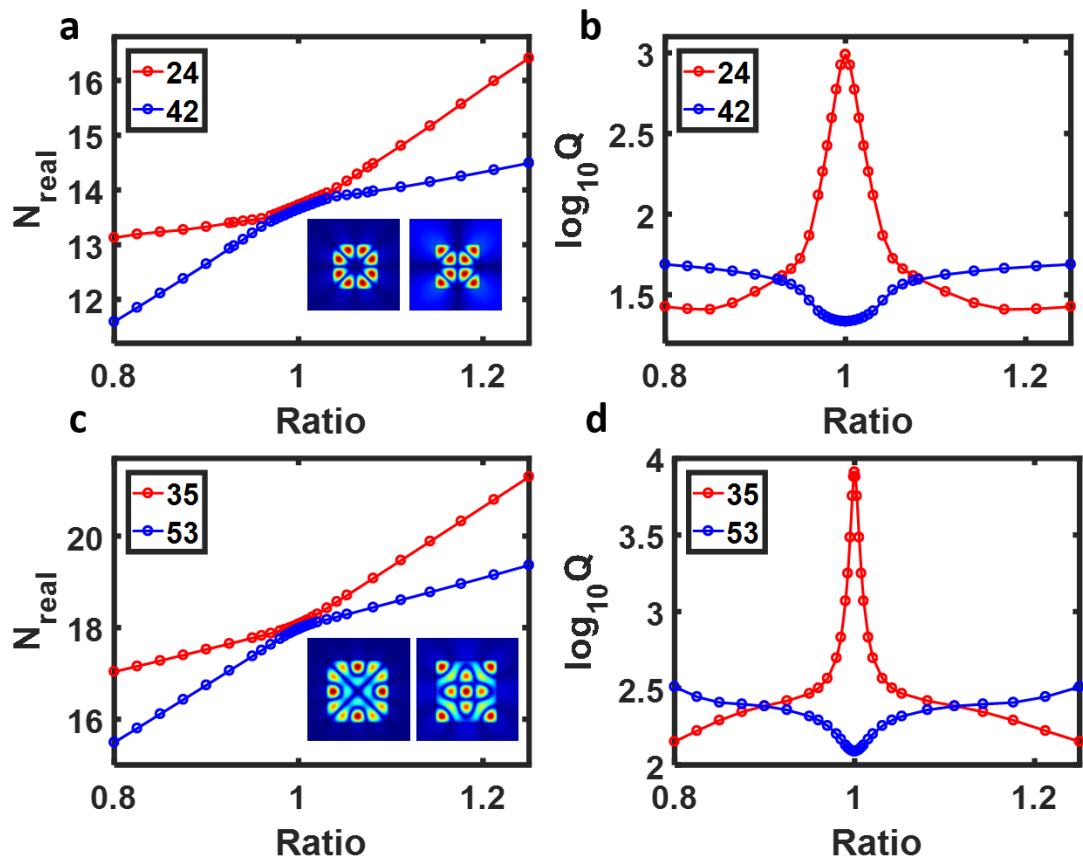


Figure S13. a-b, Real part and Q factor of eigenvalue for modes TM(2, 4) and TM(4,2) versus size ratio R . c-d, Real part and Q factor of eigenvalue for modes TM(3, 5) and TM(5,3) versus size ratio R .

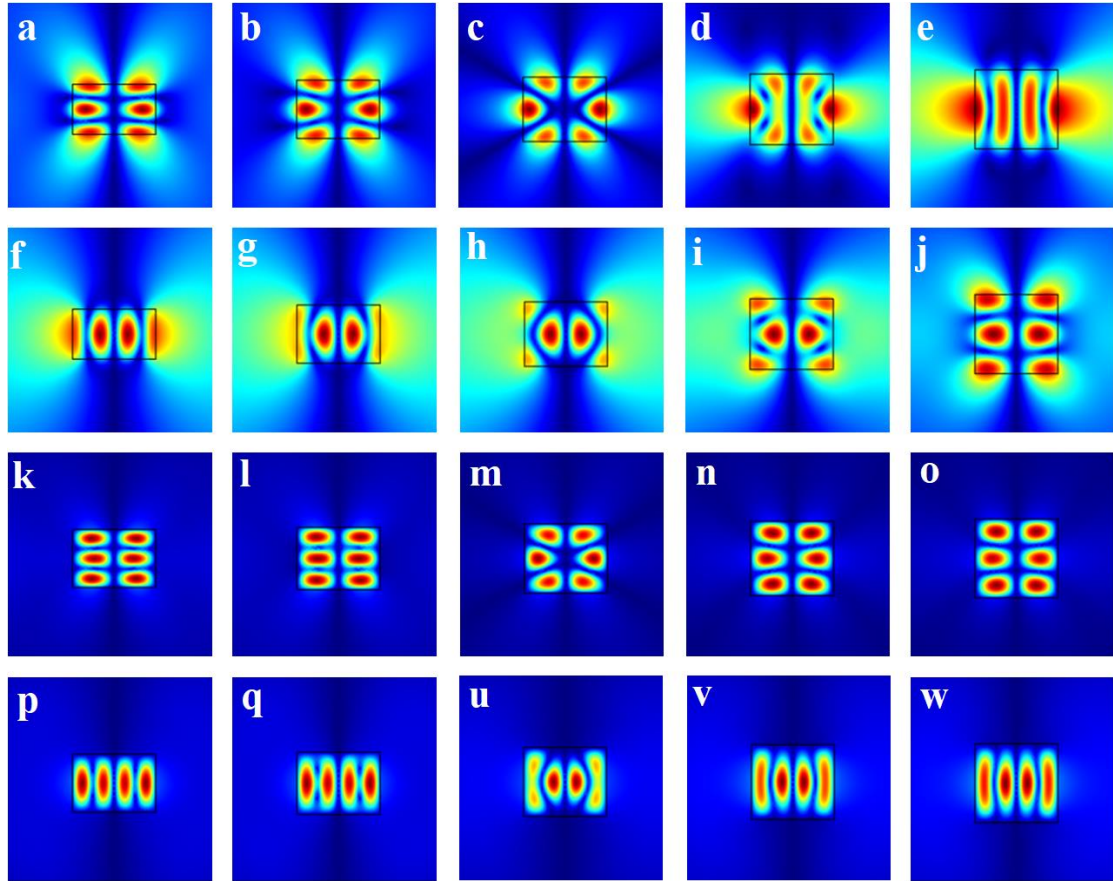


Figure S14. Mode profile evolution as function of size ratio for TE and TM cases.
a-e, $|E_z|$ of TE(2,3) at $R=0.60, 0.70, 0.775, 0.850, 0.950$. **f-j**, $|E_z|$ of TE(4,1) at $R=0.60, 0.70, 0.775, 0.850, 0.950$. **k-o**, $|H_z|$ of TM(2,3) at $R=0.70, 0.75, 0.83, 0.90, 0.95$. **p-w**, $|H_z|$ of TM(4,1) at $R=0.70, 0.75, 0.83, 0.90, 0.95$.

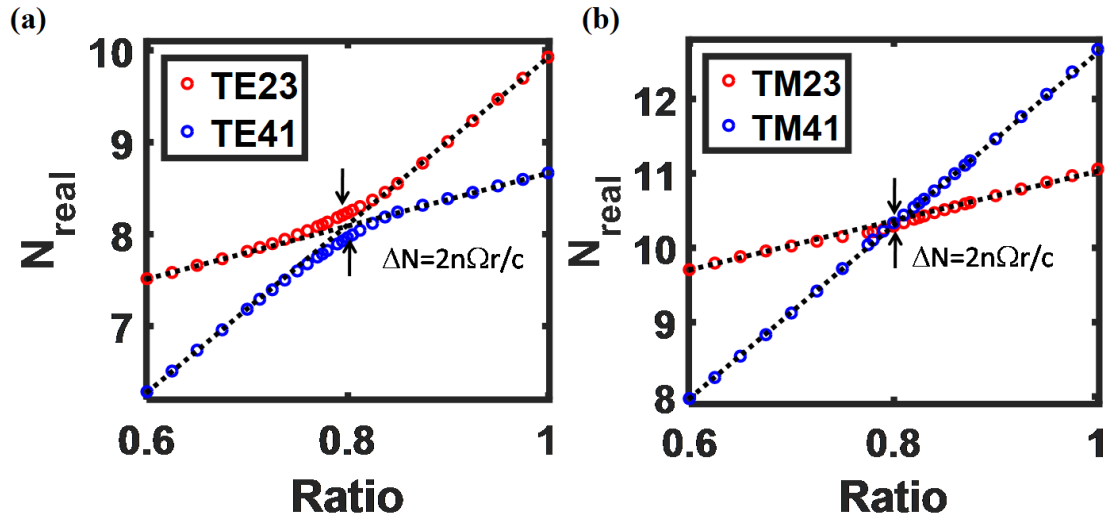


Figure S15. Coupling between high and low Q modes. **a**, Coupling strength between modes TE(2,3) and TE(4,1). **b**, Coupling strength between modes TM(2,3) and TM(4,1).

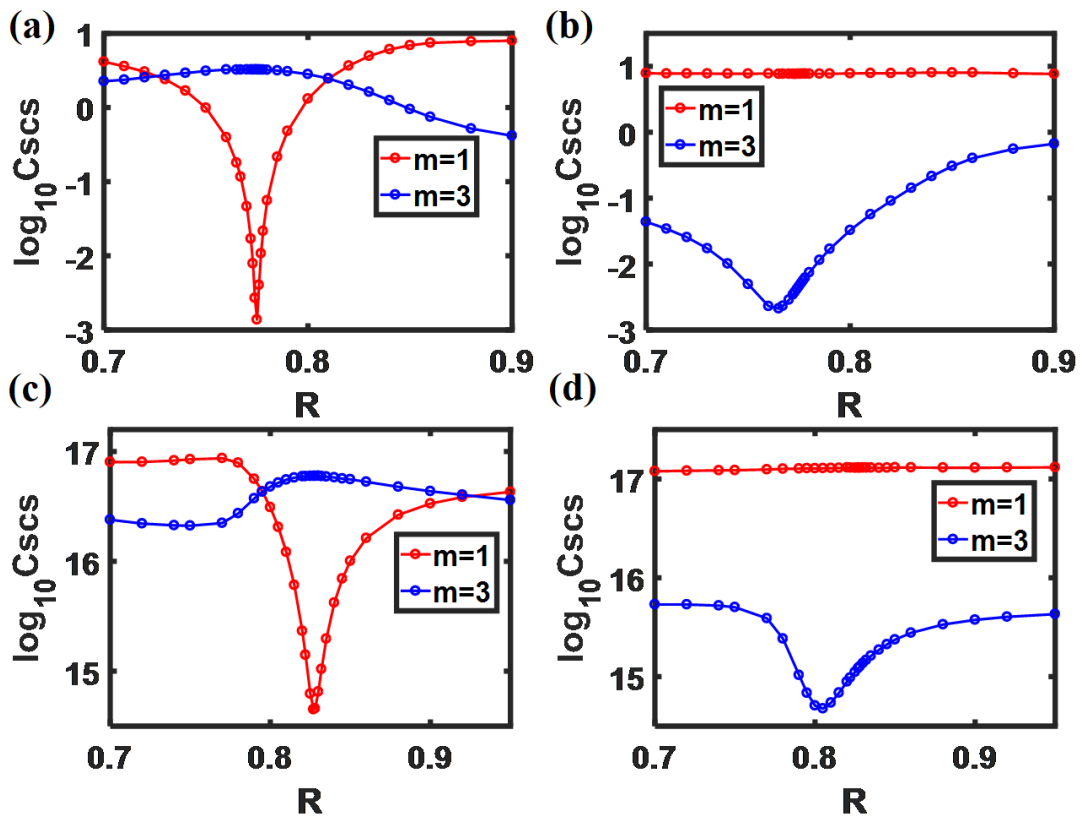


Figure S16. Multipole Analysis on high Q and low Q mode. **a-b**, Multipole decomposition of TE(2,3) and TE(4,1). **c-d**, Multipole decomposition of TM(2,3) and TM(4,1).

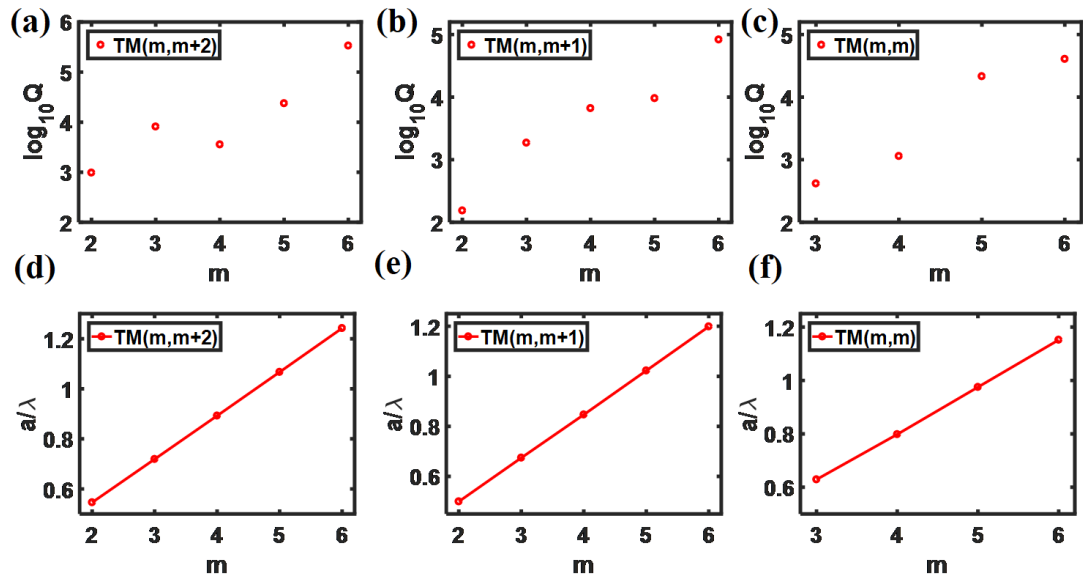


Figure S17. Q factor and a/λ . a-c, Q factor versus m for high Q modes $TM(m, m+2)$, $TM(m, m+1)$ and $TM(m, m)$. d-f, a/λ versus m for high Q modes $TM(m, m+2)$, $TM(m, m+1)$ and $TM(m, m)$.

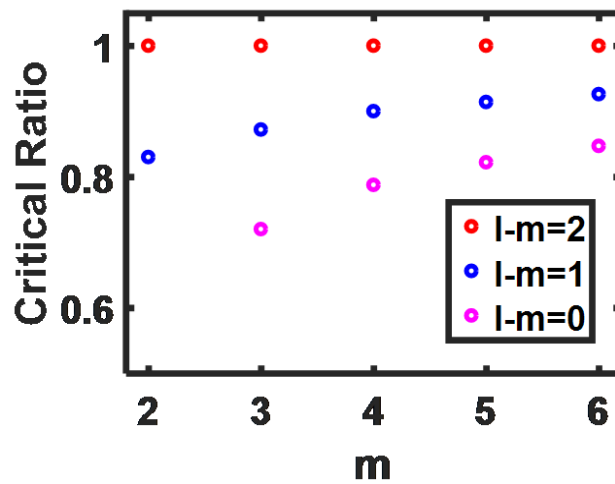


Figure.S18 critical ratio of high Q mode as function of mode order m for modes $TM(m, m+2)$, $TM(m, m+1)$ and $TM(m, m)$.

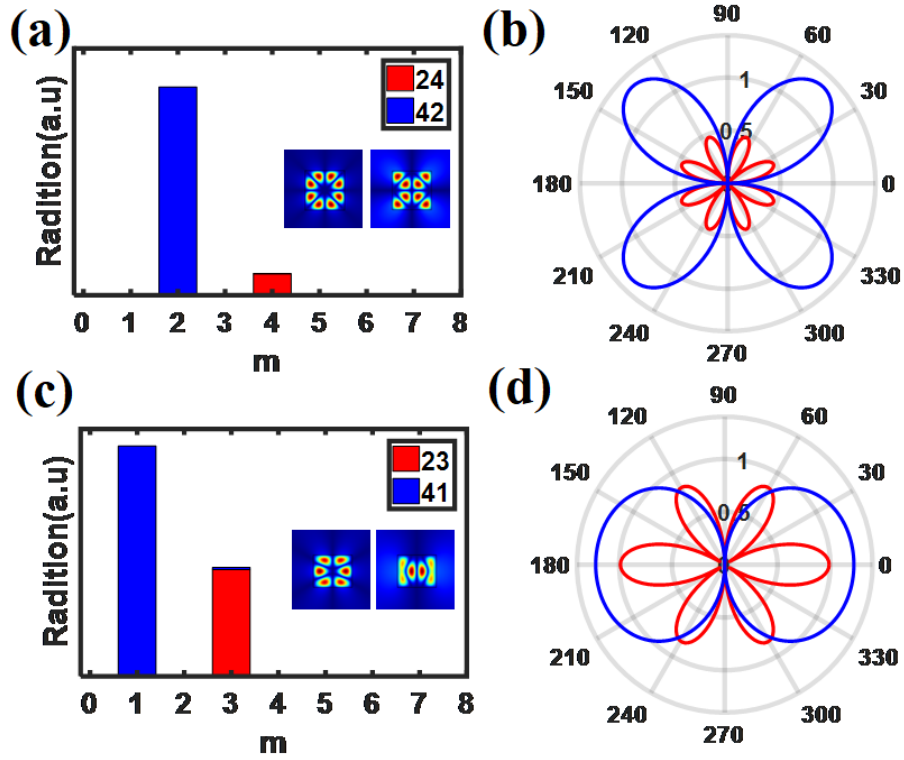


Figure S19. Multipole analysis on the high Q mode for TM case. a, Multipole analysis on the high and low Q mode TM(2,4) and TM(4,2). b, Fourier transformed $E(k_0)$ modes TM(2,4) and TM(4,2). c, Multipole analysis on the high and low Q mode TM(2,3) and TM(4,1). d, Fourier transformed $E(k_0)$ modes TM(2,3) and TM(4,1).

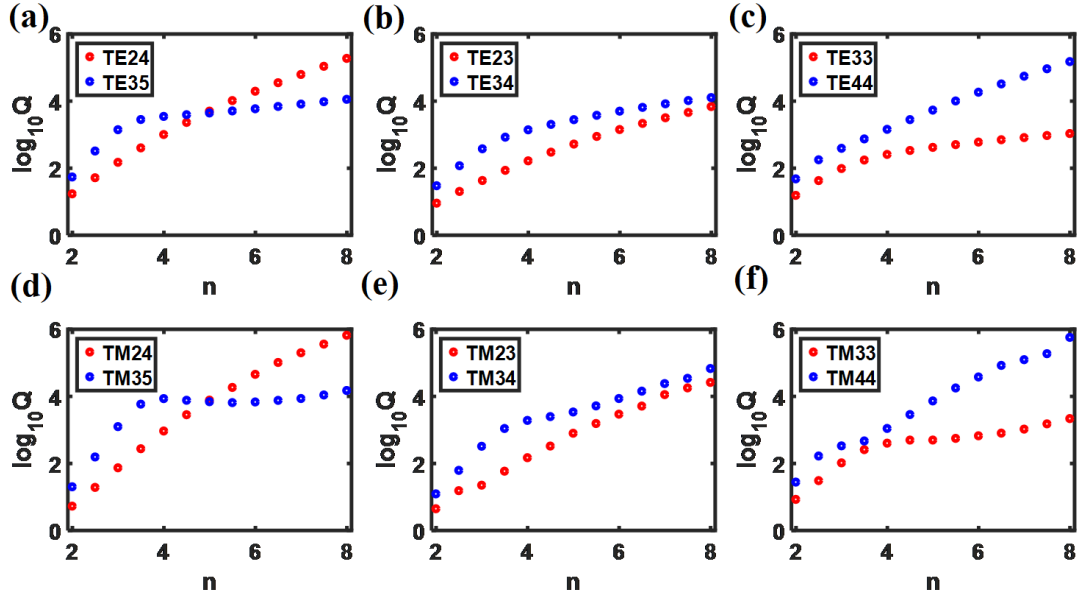


Figure S20. High Q mode property as function of refractive index. **a**, Q factor versus n for TE(2,4) and TE(3,5). **b**, Q factor versus n for TE(2,3) and TE(3,4). **c**, Q factor versus n for TE(3,3) and TE(4,4). **d**, Q factor versus n for TM(2,4) and TM(3,5). **e**, Q factor versus n for TM(2,3) and TM(3,4). **f**, Q factor versus n for TM(3,3) and TM(4,4).

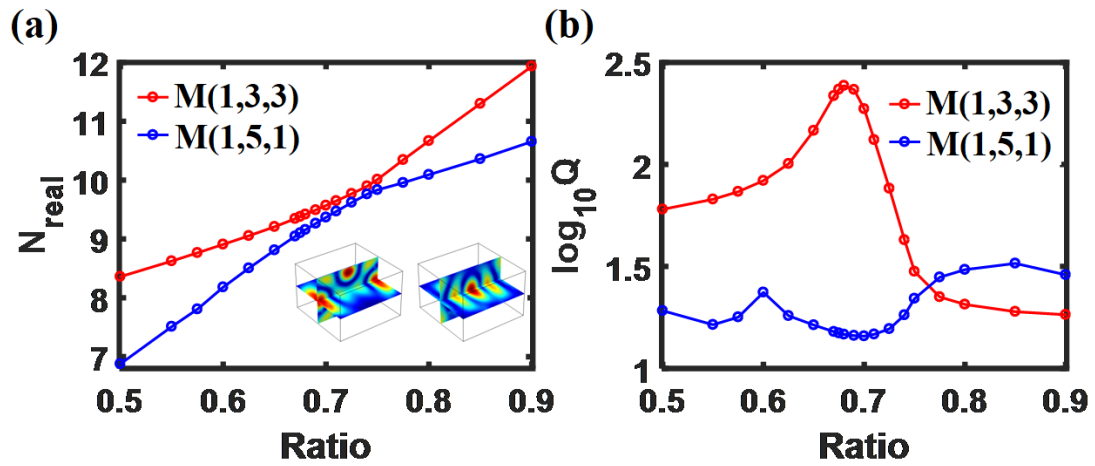


Figure S21 High Q modes in single cuboid. a-b, N_{real} (a) and Q factor (b) versus size ratio for magnetic modes M(1,3,3) and M(1,5,1).

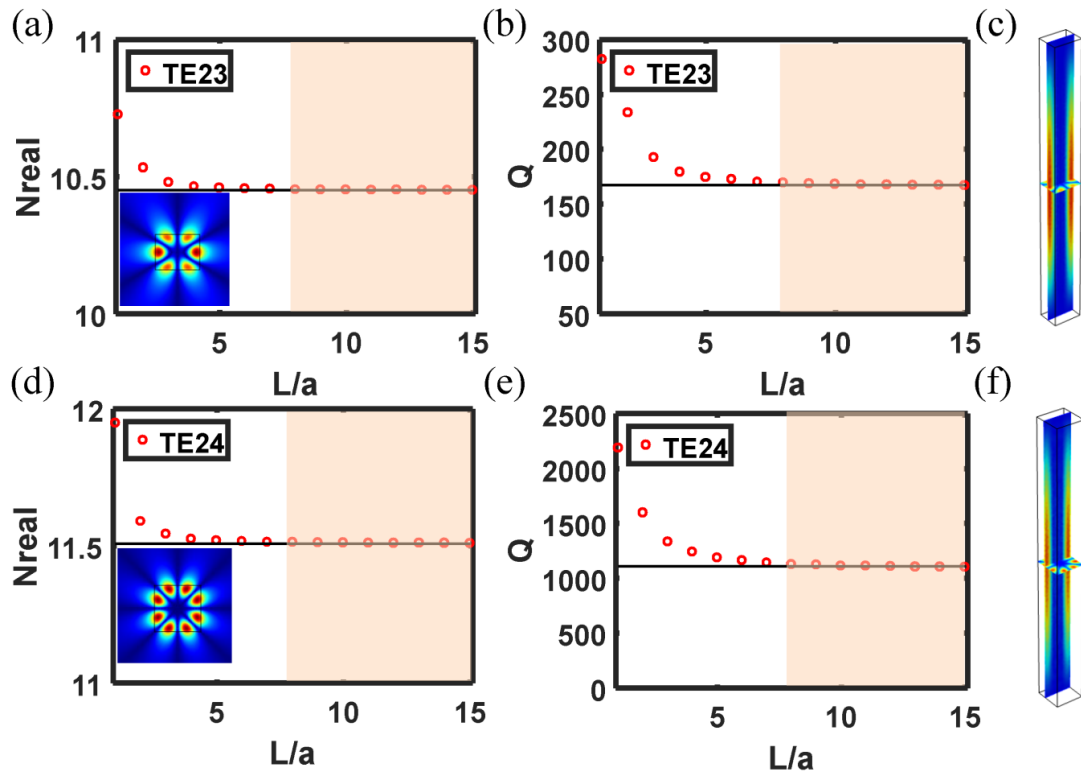


Figure S22 Length effect of nanowire axis on eigenvalue of leaky modes for NW. (a) Real part of eigenvalue for mode TE(2,3) versus L/a for $R=0.775$ while black solid line represents 2D calculation and red dot represents 3D calculation; (b) Q-factor for mode TE(2,3) versus L/a ; (c) Eigenfield distribution for TE(2,3) while the length of NW is finite; (d) Real part of eigenvalue for mode TE(2,4) versus L/a for $R=1.00$ while black solid line represents 2D calculation and red dot represents 3D calculation; (e) Q-factor for mode TE(2,4) versus L/a ; (f) Eigenfield distribution for TE(2,3) while the length of NW is finite;

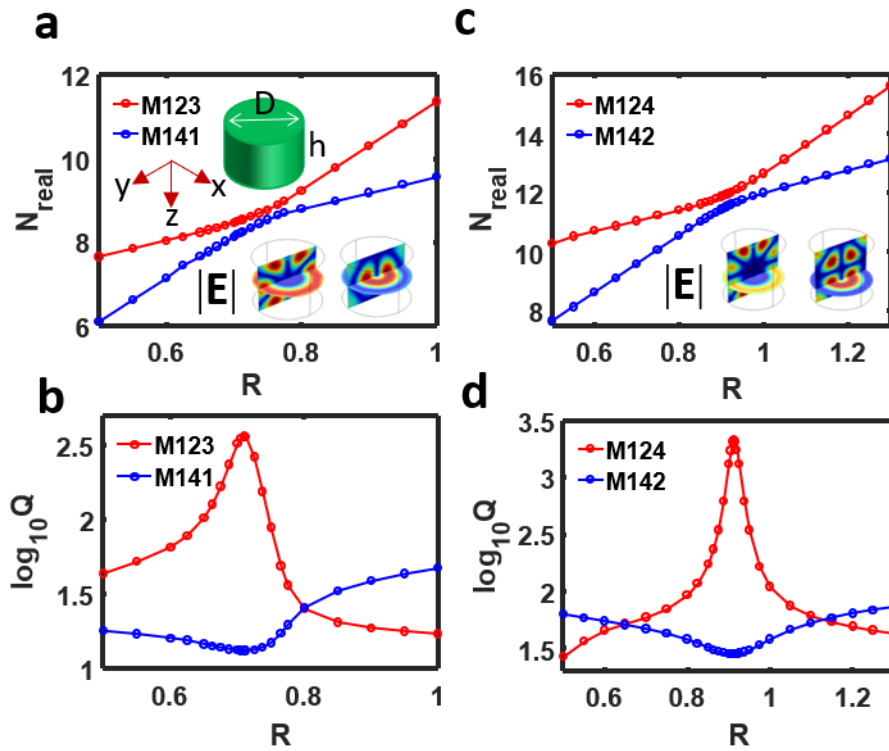


Figure S23 Magnetic high-Q modes in single disk. a-b, N_{real} (a) and Q factor (b) versus size ratio for magnetic modes M(1,2,3) and M(1,4,1). c-d, N_{real} (c) and Q factor (d) versus size ratio for magnetic modes M(1,2,4) and M(1,4,2).

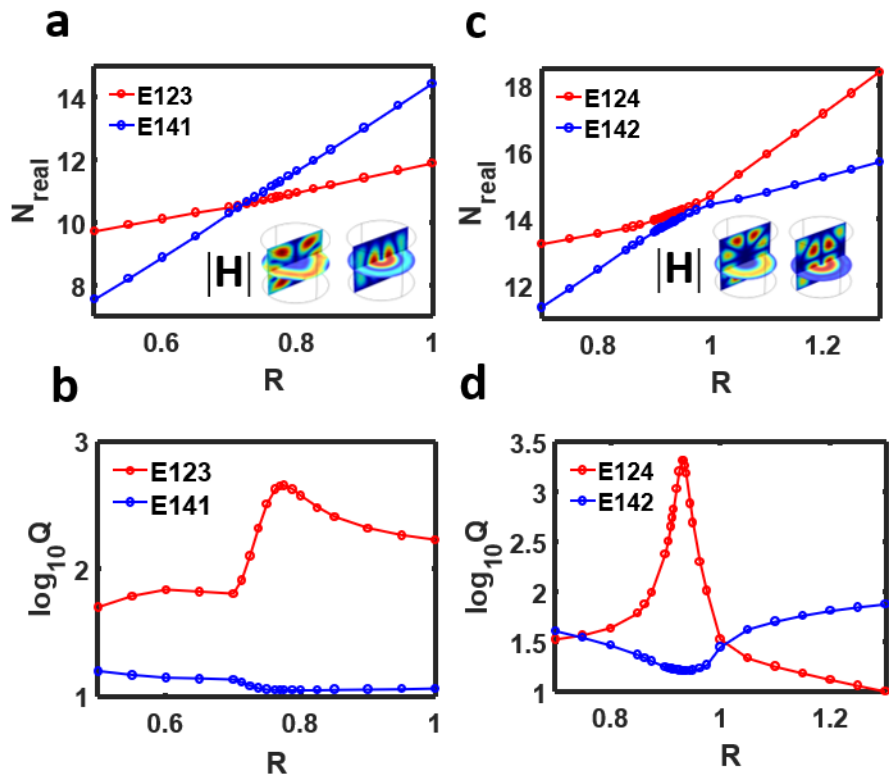


Figure S24 Electric high-Q modes in single disk. a-b, N_{real} (a) and Q factor (b) versus size ratio for magnetic modes E(1,2,3) and E(1,4,1). c-d, N_{real} (c) and Q factor (d) versus size ratio for magnetic modes E(1,2,4) and E(1,4,2).

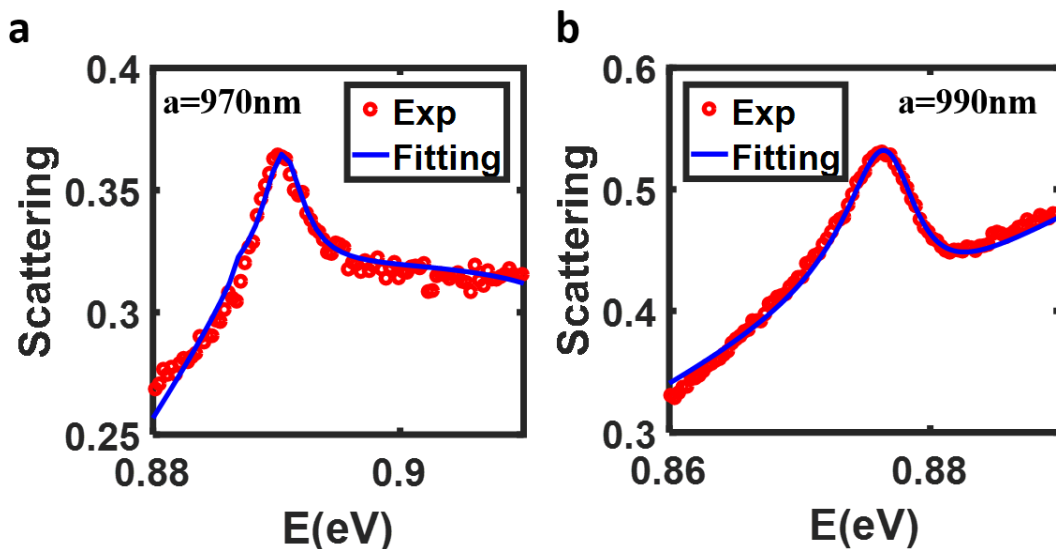


Figure S25. a, Fano fitting for $a=970\text{nm}$. b, Fano fitting for $a=990\text{nm}$.

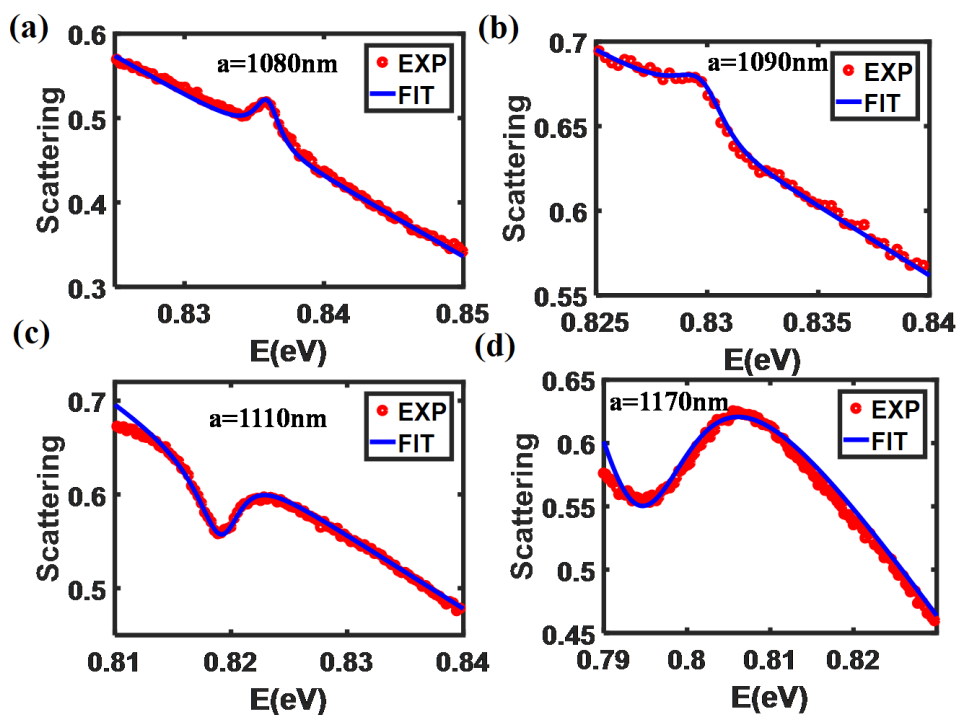


Figure S26. Typical Examples of Fano resonance fitting of scattering spectrum for rectangular NW with different width. a, $a=1080\text{nm}$. b, $a=1090\text{nm}$. c, $a=1110\text{nm}$. d, $a=1170\text{nm}$.

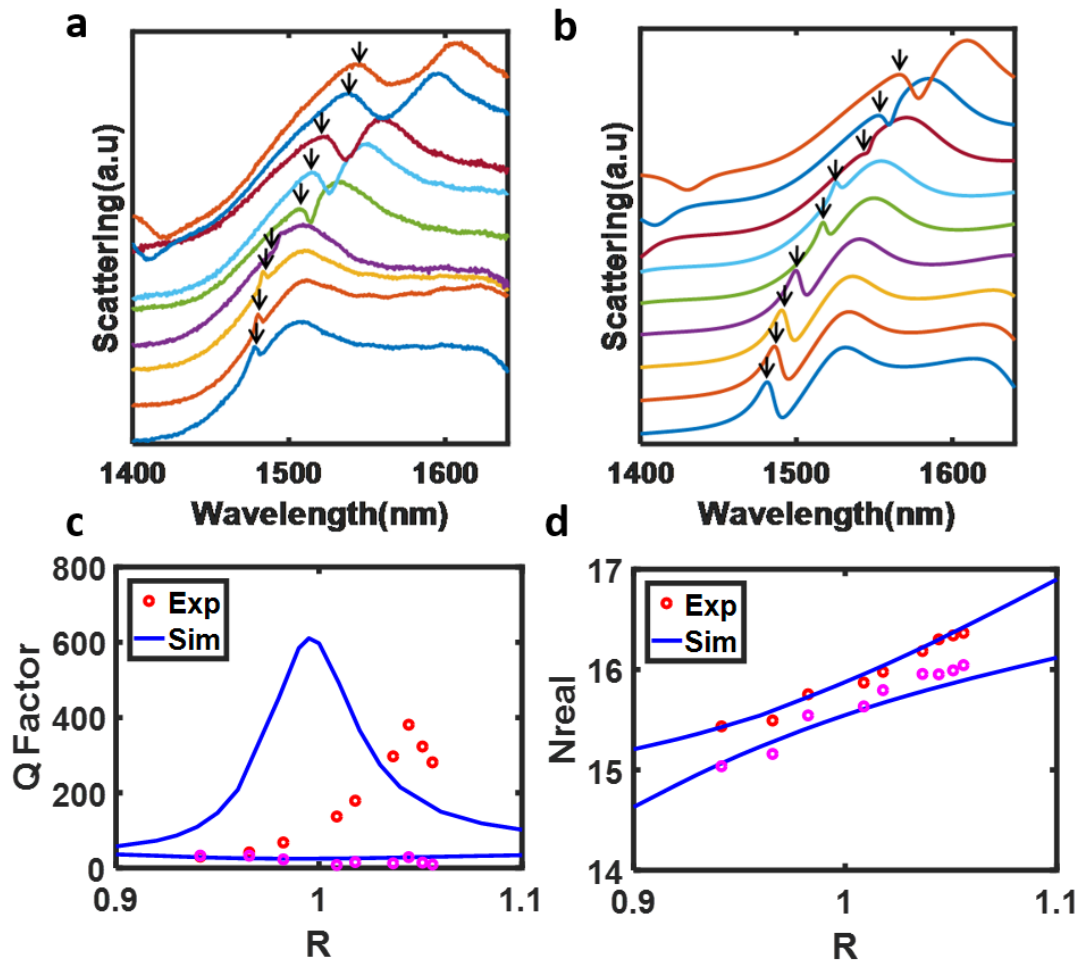


Figure S27. Experimental verification of high Q mode TE(3,5) in single silicon NW for TE Case. a-b, Measured and numerically calculated scattering spectrum for single NW with different width while the thickness of NW is fixed as 1130nm. c-d, Extracted Q factor.

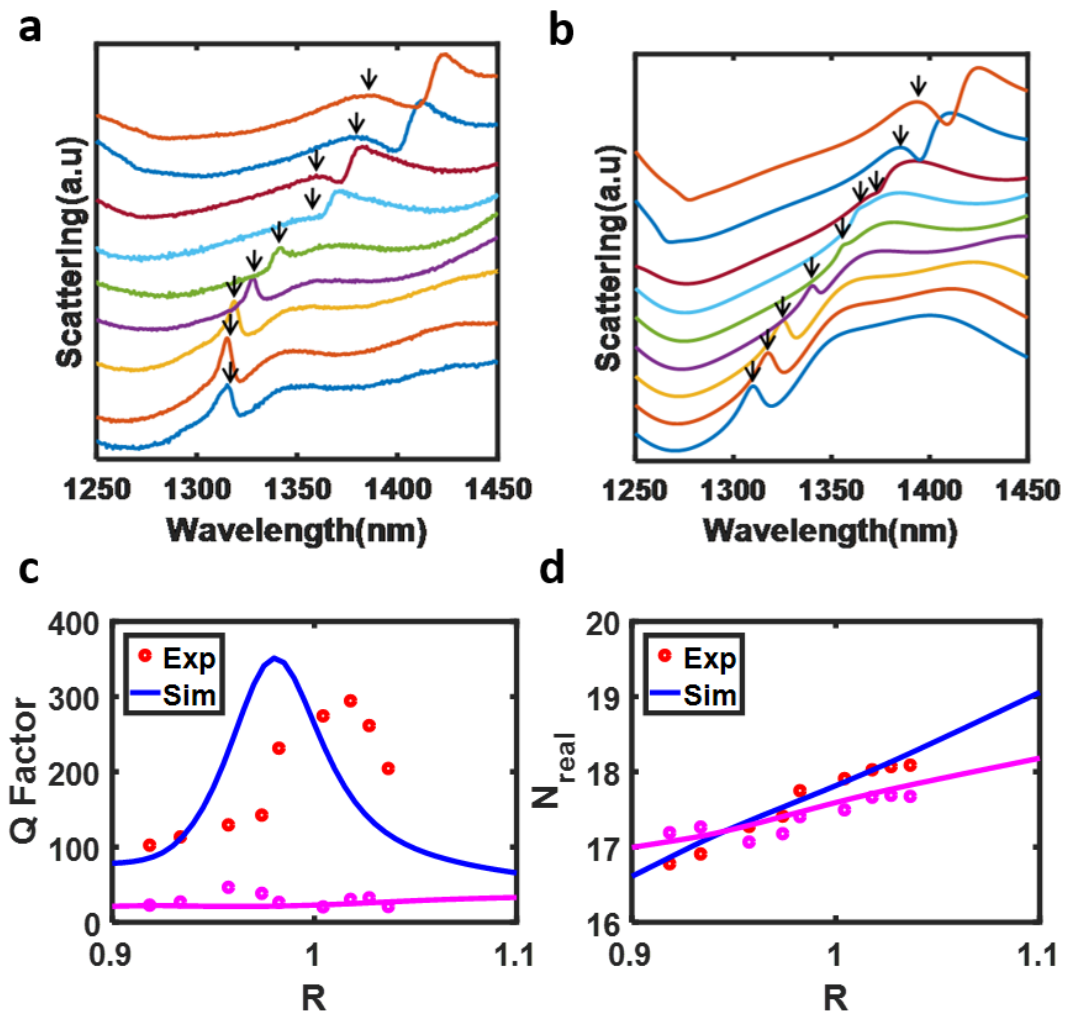


Figure S28. Experimental verification of high Q mode TM(3,5) in single silicon NW for TM Case. a-b, Measured and numerically calculated scattering spectrum for single NW with different width while the thickness of NW is fixed as 1130nm. c-d, Extracted Q factor and N_{real} versus R.

References

14. Wiersig, J. Formation of long-lived, scarlike modes near avoided resonance crossings in optical microcavities. *Phys. Rev. Lett.* **97**, 1–4 (2006).
28. Wiersig, J. Hexagonal dielectric resonators and microcrystal lasers. *Phys. Rev. A - At. Mol. Opt. Phys.* **67**, 12 (2003).
32. Miroshnichenko, A. E., Flach, S. & Kivshar, Y. S. Fano resonances in nanoscale structures. *Rev. Mod. Phys.* **82**, 2257–2298 (2010).